

Research Article

Reactive Power Control of Single-Stage Three-Phase Photovoltaic System during Grid Faults Using Recurrent Fuzzy Cerebellar Model Articulation Neural Network

Faa-Jeng Lin, Kuang-Chin Lu, and Hsuan-Yu Lee

Department of Electrical Engineering, National Central University, Chungli 320, Taiwan

Correspondence should be addressed to Faa-Jeng Lin; linfj@ee.ncu.edu.tw

Received 15 June 2014; Accepted 27 July 2014; Published 24 August 2014

Academic Editor: Franca Morazzoni

Copyright © 2014 Faa-Jeng Lin et al. This is an open access article distributed under the Creative Commons Attribution License, which permits unrestricted use, distribution, and reproduction in any medium, provided the original work is properly cited.

This study presents a new active and reactive power control scheme for a single-stage three-phase grid-connected photovoltaic (PV) system during grid faults. The presented PV system utilizes a single-stage three-phase current-controlled voltage-source inverter to achieve the maximum power point tracking (MPPT) control of the PV panel with the function of low voltage ride through (LVRT). Moreover, a formula based on positive sequence voltage for evaluating the percentage of voltage sag is derived to determine the ratio of the injected reactive current to satisfy the LVRT regulations. To reduce the risk of overcurrent during LVRT operation, a current limit is predefined for the injection of reactive current. Furthermore, the control of active and reactive power is designed using a two-dimensional recurrent fuzzy cerebellar model articulation neural network (2D-RFCMANN). In addition, the online learning laws of 2D-RFCMANN are derived according to gradient descent method with varied learning-rate coefficients for network parameters to assure the convergence of the tracking error. Finally, some experimental tests are realized to validate the effectiveness of the proposed control scheme.

1. Introduction

The cerebellar model articulation neural network (CMANN) is a lookup-table based neural network which can be thought of as a learning mechanism that simulates mammalian cerebellum. Basically, the input space of the CMANN is divided into discrete states, which are called elements. Moreover, several elements construct a block and an overlapped area formed by quantized blocks is called hypercube. Different hypercubes can be obtained by shifting each block a small interval. Furthermore, the CMANN assigns each hypercube to a memory cell for storing learning information. To obtain the output of the CMANN for given input data, only the hypercubes covering the input data will be activated and effectively contribute to the corresponding output. The basic concept of the CMANN is to store learned data into hypercubes and the data can easily be recalled with less occupied storage space. Consequently, the behavior of storing the learned information in the CMANN is similar to the

action of the cerebellar in mammalian. Advantages of the CMANN include fast learning, good localization capability, and simplicity of computation [1]. However, in the general CMANN, there are only two kinds of states in the mapped area of the state space, that is, 1 and 0. This directly affects the generalization capability of CMANN and may result in discontinuous output [2, 3]. In order to acquire the derivative information of input and output variables, a CMANN with a differentiable Gaussian receptive field basis function has been proposed in [4]. Due to the lack of time-delayed feedback in its inherent feedforward neural network structure, the application domain of CMANN is limited to static mapping problems. In addition, a recurrent fuzzy CMANN (RFCMANN) with Gaussian receptive field basis function was proposed in [5] to overcome the aforementioned disadvantage of CMANN. In this study, a two-dimensional RFCMANN (2D-RFCMANN) with Gaussian basis function control scheme is proposed for the active and reactive power control of the single-stage three-phase grid-connected photovoltaic (PV)

system. The first dimension of the 2D-RFCMANN is for the tracking error input and the second dimension of the 2D-RFCMANN is for the derivative of the tracking error input.

The penetration of renewable energy sources has increased significantly because of raising awareness of the environmental issues and the deregulation of the electric power distribution industry. Among these renewable energy sources, PV system is one of the main candidates to play an important role in the future of power distribution. However, the connection of a large number of distributed energy sources (DESSs) to the electrical power grid can cause instability when electrical disturbances appear in the grid. One of the most challenging disturbances is the voltage sags [6, 7]. The sources of the voltage sags are various such as short circuits between phases or phases and ground, lightning, and overloads. To minimize the negative effects of a large number of DESSs on the reliability of the power grids, different countries have defined various low voltage ride through (LVRT) regulations for DESSs. E.ON has defined the voltage profile of the low voltage ride through (LVRT) at the grid connection for type-2 generating plants [8]. Grid regulations require that the DESSs have to inject reactive current to support grid stability during grid faults [8], in which 1 pu of reactive current is required as the depth of the sag reaches 50%. In this study, the E.ON LVRT regulation is adopted to determine the ratio of the required reactive current during grid faults.

The asymmetrical grid voltage sags will worsen the performance of the grid-connected inverter (GCI) especially the degradation of the power quality caused by the power ripple and the increase of current harmonic distortion. In order to overcome these disadvantages, some control methods based on symmetric components have been proposed to deal with unbalanced grid faults [9–13]. A control scheme which can adjust the characteristics of power quality by using two adjustable control parameters was developed in [9]. In [10], a selective active power quality control based on various current reference generating methods was proposed. Reference [11] has proposed a control method to minimize the peak value of the injection current during the voltage sag. In [12], a positive and negative sequences current injection method was proposed to provide the active power and reactive current without exceeding the current limit of inverter. The flexible reactive current injection scheme introduced in [13] provides voltage support during voltage sag by injecting reactive current via both positive and negative sequences. However, the aforementioned control methods principally focus on the power control of grid-connected inverter, whereas the fulfillment of the LVRT requirement and the control of the power flow between the dc-link bus and ac grid during grid faults are not well explored. In this study, the 2D-RFCMANN control scheme is proposed to control not only the output voltage of the PV panel via the maximum power point tracking (MPPT) in normal condition, but also the reactive power based on LVRT requirement with considering the power balance between dc-link bus and ac grid during grid faults.

In this study, the analysis of the instantaneous active/reactive output power of the three-phase GCI during

grid faults is carried out by using symmetric component method. The MPPT control of PV system is also considered to ensure the power balance during grid faults. Subsequently, the dual second-order generalized integrator phase-locked loop (DSOGI-PLL) method [10, 14, 15] is adopted for synchronizing the GCI to the grid. Moreover, a new formula which is based on the positive sequence voltage is derived to evaluate the percentage of voltage sag and to determine the injected currents during the grid faults. Furthermore, the network structure and online training algorithms of network parameters of the proposed 2D-RFCMANN for the active and reactive power control are discussed in detail. Furthermore, two types of grid faults are tested and discussed to evaluate the performance of the proposed control scheme. The paper is organized as follows. In Section 2, the grid-connected PV system is introduced. In Section 3, the instantaneous active/reactive power formulation, DSOGI-PLL synchronization mechanism, and the control strategy of the grid-connected PV system during grid faults are discussed. The 2D-RFCMANN is presented in Section 4. In Section 5, the features of the proposed control scheme are examined by some experimental results. Finally, Section 6 draws the conclusions.

2. System Description

Figure 1 shows the block diagrams of the proposed single-stage three-phase grid-connected PV system. The behavior of the PV panel is emulated by a Chroma 62100H-600S PV panel simulator operating at 203 Vdc output voltage with maximum output power 1 kW. The power grid was emulated by three programmable 2 kVA single-phase KIKUSUI PCR2000LE AC power supplies feeding a Y-connected 100 Ω /phase resistive load and connected to the GCI with a 3 kVA Y- Δ transformer. The 2 kVA three-phase GCI, with output 110 Vrms line to line voltage, is connected to the PV panel simulator through a dc-link capacitor and connected to the Y- Δ transformer with three 10 mH/phase coupling inductors. The switching frequency $f_{sw,GCI}$ of the three-phase GCI is set at 10 kHz. Table 1 shows the parameters of the experimental setup. Moreover, the control system is installed on a desktop personal computer (PC) which includes an A/D converter card (PCI-1716), a PC-based control system, and a D/A converter card (MRC-6810). In the PC-based control system, the SIMULINK control package is adopted for the implementation of the proposed algorithms of the MPPT and LVRT control. The analog input signals include output voltage V_{pv} and current I_{pv} of the PV panel simulator, the output line voltages v_{ab} , v_{bc} , and v_{ca} , and line currents i_a , i_b , and i_c of the GCI. The control output of the PC-based control system is the three-phase reference currents of GCI i_a^* , i_b^* , and i_c^* . Furthermore, the emulated faults occur at the point of common coupling (PCC).

In Figure 1, the output currents of the GCI are controlled by the maximum power point (MPP) voltage V_{pv}^* in the normal condition. The adopted MPPT method is the incremental conductance (IC) method with a fixed incremental step size set for the voltage [16]. Moreover, if a grid fault occurs at the

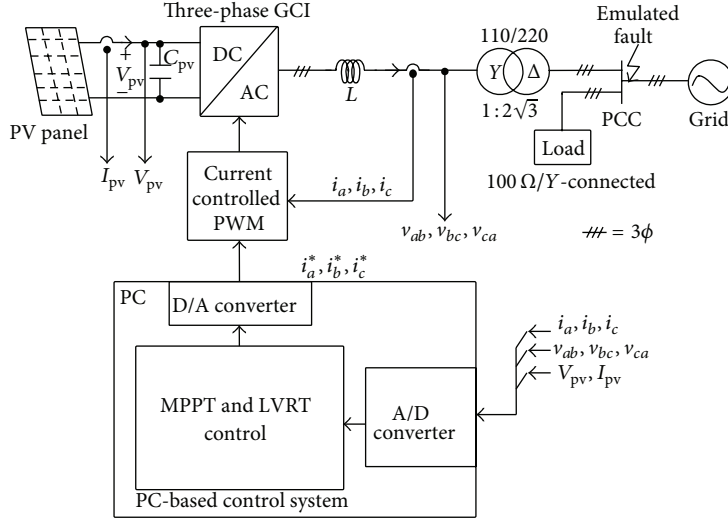


FIGURE 1: Block diagrams of experimental single-stage three-phase grid-connected PV system.

TABLE 1: Parameters of experimental setup.

Dc-link capacitor	C_{pv}	3360 mF
Grid connection inductor	L	10 mH
Inverter output voltage	v_{ab}, v_{bc}, v_{ca}	110 Vrms line to line, 60 Hz
Inverter maximum current	I_{max}	5 Arms (7.1 A peak current)
Emulated PV panel		V_{oc} : 236 V, I_{sc} : 6.0 A, 1 kW
Switching frequency	f_{sw_GCI}	10 kHz

PCC, the fault voltages at the GCI terminals appear differently from the fault voltages at the PCC [6, 7]. Furthermore, in the normal condition of the grid, the GCI regulates the active power injecting into the grid and maintains the V_{pv} voltage so as to track the MPP for maximizing the energy extraction. On the other hand, in the fault conditions of the grid, the reactive power control can mitigate the effects of voltage sag by injecting additional reactive current to the grid to ride through the perturbation and support the grid voltage. In addition, the injecting current has to meet the LVRT regulations, without going beyond the GCI current limit I_{max} simultaneously.

3. Reactive Power Control Strategy during Grid Faults

3.1. Instantaneous Power Formulation under Grid Fault Conditions. For a three-phase GCI, the instantaneous active and reactive power outputs at the grid connection point are described as follows [17]:

$$P = \mathbf{v} \cdot \mathbf{i} = v_a i_a + v_b i_b + v_c i_c, \quad (1)$$

$$Q = \mathbf{v} \times \mathbf{i} = \mathbf{v}_\perp \cdot \mathbf{i} \\ = \frac{1}{\sqrt{3}} [(v_a - v_b) i_c + (v_b - v_c) i_a + (v_c - v_a) i_b], \quad (2)$$

where $\mathbf{v}_\perp = (1/\sqrt{3}) \begin{bmatrix} 0 & 1 & -1 \\ -1 & 0 & 1 \\ 1 & -1 & 0 \end{bmatrix} \mathbf{v}$, $\mathbf{v} = [v_a \ v_b \ v_c]^T$, and $\mathbf{i} = [i_a \ i_b \ i_c]^T$ represent the three phase voltages and currents of the GCI, respectively; P and Q represent the instantaneous active and reactive power outputs of the GCI, respectively. In (1) and (2), \mathbf{v}_\perp and \mathbf{v} are orthogonal only when the three voltages of \mathbf{v} are balanced. The asymmetric three-phase voltage and current vector are represented as

$$\mathbf{v} = \mathbf{v}^+ + \mathbf{v}^-, \quad (3) \\ \mathbf{i} = \mathbf{i}^+ + \mathbf{i}^-,$$

where $\mathbf{v}^+ = [v_a^+ \ v_b^+ \ v_c^+]^T$ and $\mathbf{v}^- = [v_a^- \ v_b^- \ v_c^-]^T$ represent the positive and negative sequences of \mathbf{v} , respectively; $\mathbf{i}^+ = [i_a^+ \ i_b^+ \ i_c^+]^T$ and $\mathbf{i}^- = [i_a^- \ i_b^- \ i_c^-]^T$ represent the positive and negative sequences of \mathbf{i} , respectively. Note that the zero sequence of \mathbf{v} and \mathbf{i} does not exist due to the three-phase three-wire AC system configuration of the GCI. As a result, P and Q in (1) and (2) can be rewritten as

$$P = \mathbf{v} \cdot \mathbf{i} = (\mathbf{v}^+ + \mathbf{v}^-) \cdot (\mathbf{i}^+ + \mathbf{i}^-) \\ = \mathbf{v}^+ \cdot \mathbf{i}^+ + \mathbf{v}^- \cdot \mathbf{i}^- + \mathbf{v}^+ \cdot \mathbf{i}^- + \mathbf{v}^- \cdot \mathbf{i}^+, \quad (4)$$

$$Q = \mathbf{v}_\perp \cdot \mathbf{i} = (\mathbf{v}_\perp^+ + \mathbf{v}_\perp^-) \cdot (\mathbf{i}^+ + \mathbf{i}^-) \\ = \mathbf{v}_\perp^+ \cdot \mathbf{i}^+ + \mathbf{v}_\perp^- \cdot \mathbf{i}^- + \mathbf{v}_\perp^+ \cdot \mathbf{i}^- + \mathbf{v}_\perp^- \cdot \mathbf{i}^+, \quad (5)$$

where the corresponding orthogonal vectors in (5) can be derived by using the matrix transformation in (2). Thus, the

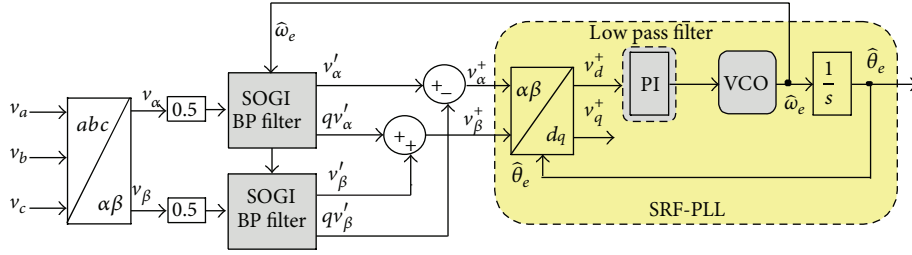


FIGURE 2: Schematic diagram of DSOGI-PLL.

instantaneous active and reactive output power of the GCI can be obtained by using (4) and (5) under both normal and abnormal conditions of the grid.

3.2. Grid Synchronization of GCI. The active and reactive power control of the GCI is based on a synchronous reference frame (SRF) with proportional-integral (PI) or 2D-RFCMANN controllers. Moreover, it is important to detect the phase angle of the voltage at PCC in order to synchronize with the grid during grid faults. At present, the most popular PLL structure is the synchronous reference frame PLL (SRF-PLL) [14]. The input three-phase voltages of the SRF-PLL can be given by

$$\begin{bmatrix} v_a \\ v_b \\ v_c \end{bmatrix} = |V^+| \begin{bmatrix} \sin(\theta_e) \\ \sin(\theta_e - \frac{2}{3}\pi) \\ \sin(\theta_e + \frac{2}{3}\pi) \end{bmatrix} + |V^-| \begin{bmatrix} \sin(\theta_e) \\ \sin(\theta_e + \frac{2}{3}\pi) \\ \sin(\theta_e - \frac{2}{3}\pi) \end{bmatrix}, \quad (6)$$

where $|V^+|$ and $|V^-|$ are the amplitude of the positive and negative sequence of the three-phase voltage; $\theta_e = \omega_e t$, and ω_e is the utility angular frequency. In the SRF-PLL, first, the Clarke transformation is applied to transfer the three-phase voltages from the abc natural reference frame to the $\alpha\beta$ stationary reference frame [14, 15]. v_α and v_β are the voltages of α , β axis which can be expressed as

$$\begin{aligned} \begin{bmatrix} v_\alpha \\ v_\beta \end{bmatrix} &= \sqrt{\frac{2}{3}} \begin{bmatrix} \frac{3}{2} & 0 \\ \frac{\sqrt{3}}{2} & \sqrt{3} \end{bmatrix} \begin{bmatrix} v_a \\ v_b \end{bmatrix} \\ &= \sqrt{\frac{3}{2}} |V^+| \begin{bmatrix} \sin(\theta_e) \\ -\cos(\theta_e) \end{bmatrix} + \sqrt{\frac{3}{2}} |V^-| \begin{bmatrix} \sin(\theta_e) \\ \cos(\theta_e) \end{bmatrix}. \end{aligned} \quad (7)$$

Then, (7) can be expressed in the synchronous reference frame by using Park transformation in the following [15]:

$$\begin{bmatrix} v_d \\ v_q \end{bmatrix} = \begin{bmatrix} \cos(\hat{\theta}_e) & \sin(\hat{\theta}_e) \\ -\sin(\hat{\theta}_e) & \cos(\hat{\theta}_e) \end{bmatrix} \begin{bmatrix} v_\alpha \\ v_\beta \end{bmatrix}$$

$$\begin{aligned} &= \sqrt{\frac{3}{2}} |V^+| \begin{bmatrix} \sin(\theta_e - \hat{\theta}_e) \\ -\cos(\theta_e - \hat{\theta}_e) \end{bmatrix} \\ &+ \sqrt{\frac{3}{2}} |V^-| \begin{bmatrix} \sin(\theta_e - \hat{\theta}_e) \\ \cos(\theta_e - \hat{\theta}_e) \end{bmatrix}, \end{aligned} \quad (8)$$

where v_d, v_q are the voltages of the d, q axis; $\hat{\theta}_e = \hat{\omega}_e t$, and $\hat{\omega}_e$ is the angular frequency of the dq synchronous reference frame. Suppose that $\hat{\theta}_e$ is close to θ_e , then $\sin(\theta_e - \hat{\theta}_e)$ is approximately equal to $\theta_e - \hat{\theta}_e$, and v_d is approximately equal to $(\sqrt{6}/2)[|V^+|(\theta_e - \hat{\theta}_e) + |V^-| \sin(2\theta_e)]$. The negative sequence component voltage of v_d can be filtered by using a properly designed low pass filter. The difference between θ_e and $\hat{\theta}_e$ will approach zero due to the closed-loop control of $\hat{\theta}_e$ that makes v_d approach zero. Therefore, with $\hat{\theta}_e \approx \theta_e$ in steady state, the phase angle detected by the SRF-PLL will be in phase with the input voltage vector. However, the dynamic behavior of the SRF-PLL will become poor under asymmetric grid faults [15]. In order to overcome this disadvantage of SRF-PLL, a dual second-order generalized integrator PLL (DSOGI-PLL) based on the extraction of the positive sequence has been proposed in [10, 14, 15]. Define $\mathbf{v}_{\alpha\beta}^+ = [v_\alpha^+ \ v_\beta^+]^T$ as the positive sequence voltage vector on the $\alpha\beta$ reference frame and it can be calculated as [10]

$$\mathbf{v}_{\alpha\beta}^+ = \frac{1}{2} \begin{bmatrix} 1 & -q \\ q & 1 \end{bmatrix} \begin{bmatrix} v'_\alpha \\ v'_\beta \end{bmatrix}, \quad (9)$$

where $q = e^{-j\pi/2}$ is a phase-shift operator in the time domain; v'_α and v'_β are the filtered voltages of v_α and v_β , respectively. The schematic diagram of DSOGI-PLL is shown in Figure 2, where the dual second-order generalized integrator (SOGI) in Figure 2 is used to generate v'_α, v'_β , and in-quadrature voltages qv'_α and qv'_β of v'_α and v'_β . Furthermore, v''_d and v''_q , which are depicted in Figure 2, are the positive sequence voltages on the dq synchronous reference frame. In addition, a voltage-controlled oscillator (VCO) is employed to convert the input voltage into $\hat{\omega}_e$. Finally, $\hat{\theta}_e$ is successfully obtained by DSOGI-PLL by using the positive sequence voltages.

According to [15], the instantaneous active and reactive power outputs of the GCI can be calculated by using the

voltage and current in the dq synchronous reference frame as follows:

$$Q = \frac{3}{2} (v_q i_d - v_d i_q), \quad P = \frac{3}{2} (v_d i_d + v_q i_q), \quad (10)$$

where i_d and i_q are the currents of the d, q axis. As mentioned above, an adequate tracking of the grid angular position of the SRF-PLL will make v_d approach zero. Thus, the active and reactive power outputs of the GCI can be represented as

$$Q = \frac{3}{2} v_q i_d, \quad P = \frac{3}{2} v_q i_q. \quad (11)$$

Accordingly, P and Q can be regulated by controlling i_q and i_d .

3.3. Reactive and Active Power Control during Grid Faults. The positive sequence voltages of the three-phase line voltages v_{ab}^+ , v_{bc}^+ , and v_{ca}^+ can be expressed as follows:

$$\begin{aligned} \begin{bmatrix} v_{ab}^+ \\ v_{bc}^+ \\ v_{ca}^+ \end{bmatrix} &= \frac{1}{3} \begin{bmatrix} 1 & a & a^2 \\ a^2 & 1 & a \\ a & a^2 & 1 \end{bmatrix} \begin{bmatrix} v_{ab} \\ v_{bc} \\ v_{ca} \end{bmatrix} \\ &= \sqrt{2} |V_l^+| \begin{bmatrix} \sin \theta_e \\ \sin \left(\theta_e - \frac{2\pi}{3} \right) \\ \sin \left(\theta_e + \frac{2\pi}{3} \right) \end{bmatrix}, \end{aligned} \quad (12)$$

where $|V_l^+|$ is the rms value of the magnitude of the positive sequence voltage of the three-phase line voltages and the operator a is equal to $e^{j2\pi/3}$. Since v_{ab}^+ , v_{bc}^+ , and v_{ca}^+ are symmetric and balanced, $|V_l^+|$ can be expressed as

$$|V_l^+| = \sqrt{\frac{1}{3} (v_{ab}^{+2} + v_{bc}^{+2} + v_{ca}^{+2})}. \quad (13)$$

Note that v_{ab}^+ , v_{bc}^+ , and v_{ca}^+ are equal to the magnitude of the three-phase line voltages when the line voltages are balanced. According to (12), if the line voltages are unbalanced, v_{ab}^+ , v_{bc}^+ , and v_{ca}^+ will be changed with the degree of unbalance. Therefore $|V_l^+|$ is adopted to evaluate the depth of voltage sag V_{sag} during grid faults in this study. The required percentage of compensation reactive current I_r^* during grid faults for LVRT can be expressed as a function of V_{sag} [8]:

$$I_r^* = \begin{cases} 0\%, & \text{where } V_{\text{sag}} < 0.1 \\ 200 V_{\text{sag}} \%, & \text{where } 0.1 < V_{\text{sag}} \leq 0.5 \\ 100\%, & \text{where } V_{\text{sag}} > 0.5, \end{cases} \quad (14)$$

and V_{sag} is defined as follows:

$$V_{\text{sag}} \equiv 1 - \frac{|V_l^+|}{V_{\text{base}}} \text{pu}, \quad (15)$$

where V_{base} is the base value of voltage which equals 110 Vrms in this study. The grid regulation by E.ON demands reactive current injection during fault condition to support the grid stability when V_{sag} is greater than 0.1 pu. Moreover, the apparent output power of GCI will be changed due to the voltage sag at PCC under grid faults. Therefore, it is necessary to calculate the maximum allowable apparent power in order to decide the maximum injection reactive and active power. The maximum apparent power S can be expressed as

$$S = (|v_a|_{\text{rms}} + |v_b|_{\text{rms}} + |v_c|_{\text{rms}}) I_{\text{max}}, \quad (16)$$

where I_{max} is the rms value of the GCI current limit and $|v_a|_{\text{rms}}$, $|v_b|_{\text{rms}}$, and $|v_c|_{\text{rms}}$ are the rms values of v_a , v_b , and v_c , respectively. Thus, the required injection reactive power Q^* and the allowable maximum output active power P^* of GCI as follows can be derived from (14) and (16):

$$Q^* = S I_r^*, \quad P^* = S \sqrt{1 - I_r^{*2}}. \quad (17)$$

A PV system should inject a certain reactive power in order to support the voltage sag at the PCC according to the LVRT requirements during grid faults. If P^* is greater than P , then the active power reference P_{ref} is set to equal the value of P before the grid faults. Therefore, all the power generated by the PV panel can be totally delivered into the grid during grid faults and the MPPT control can be operated to keep tracking the MPP. On the other hand, if P^* is smaller than P , then P_{ref} is set to P^* . Thus the output active power will be controlled to follow P_{ref} , and the GCI gives up tracking the MPP. Consequently, the power balance between P_{pv} and P can be held during grid faults.

4. D-RFCMANN Control Scheme

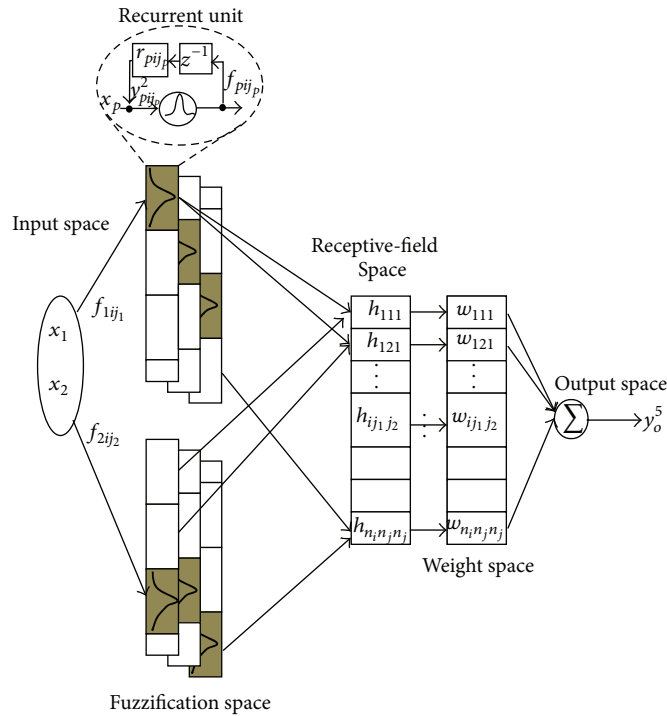
4.1. Description of 2D-RFCMANN. The structure of 2D-RFCMANN with 2 inputs and 1 output is depicted in Figure 3(a), which consists of five spaces: input space, fuzzification space, receptive-field space, weight space, and output space. Moreover, one of the fuzzy if-then rules of the proposed 2D-RFCMANN is realized as follows.

$R_{j_1 j_2}^i$: If x_1 is $f_{1i j_1}$ and x_2 is $f_{2i j_2}$, then

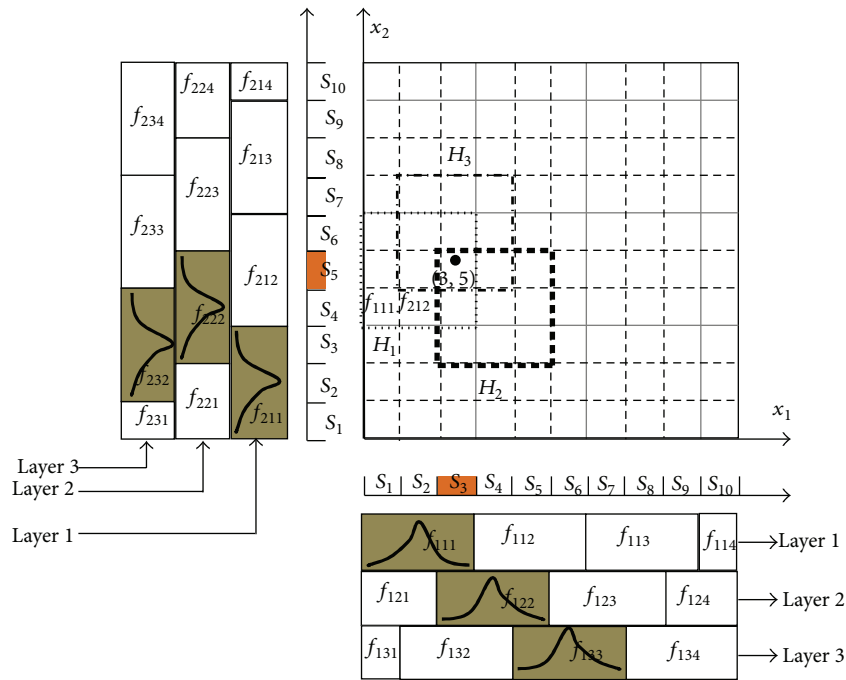
$$\begin{aligned} y_{i j_1 j_2} &= w_{i j_1 j_2} \quad \text{for } i = 1, 2, \dots, n_i; \\ j_1, j_2 &= 1, 2, \dots, n_j, \end{aligned} \quad (18)$$

where $n_i = 3$ is the number of the layers for each input dimension; $n_j = 4$ is the number of blocks for each layer; $f_{1i j_1}$ is the fuzzy set for the first input, i th layer, and j_1 th block; $f_{2i j_2}$ is the fuzzy set for the second input, i th layer, and j_2 th block; $w_{i j_1 j_2}$ is the corresponding output weight in the consequent part. Furthermore, the signal propagation and the basic function in each space of the 2D-RFCMANN are introduced as follows.

Space 1 (input space). In this space, the input variables x_1 and x_2 are both divided into n_e regions (which are called "elements"). The number of n_e represents the input resolution.



(a) Structure of 2D-RFCMANN



(b) 2D-RFCMANN with $p = 2$, $n_i = 3$, and $n_j = 4$ and its configuration of receptive-field space activated by state (3, 5)

FIGURE 3: Two-dimensional RFCMANN.

For example, a 2D-RFCMANN with $n_e = 10$ is shown as in Figure 3(b).

Space 2 (fuzzification space). According to the concept of CMANN, several elements can be accumulated as a block.

In this space, each block performs a Gaussian receptive-field basis function. The fuzzification of the corresponding membership function in the 2D-RFCMANN is realized by the Gaussian basis function which can be expressed as

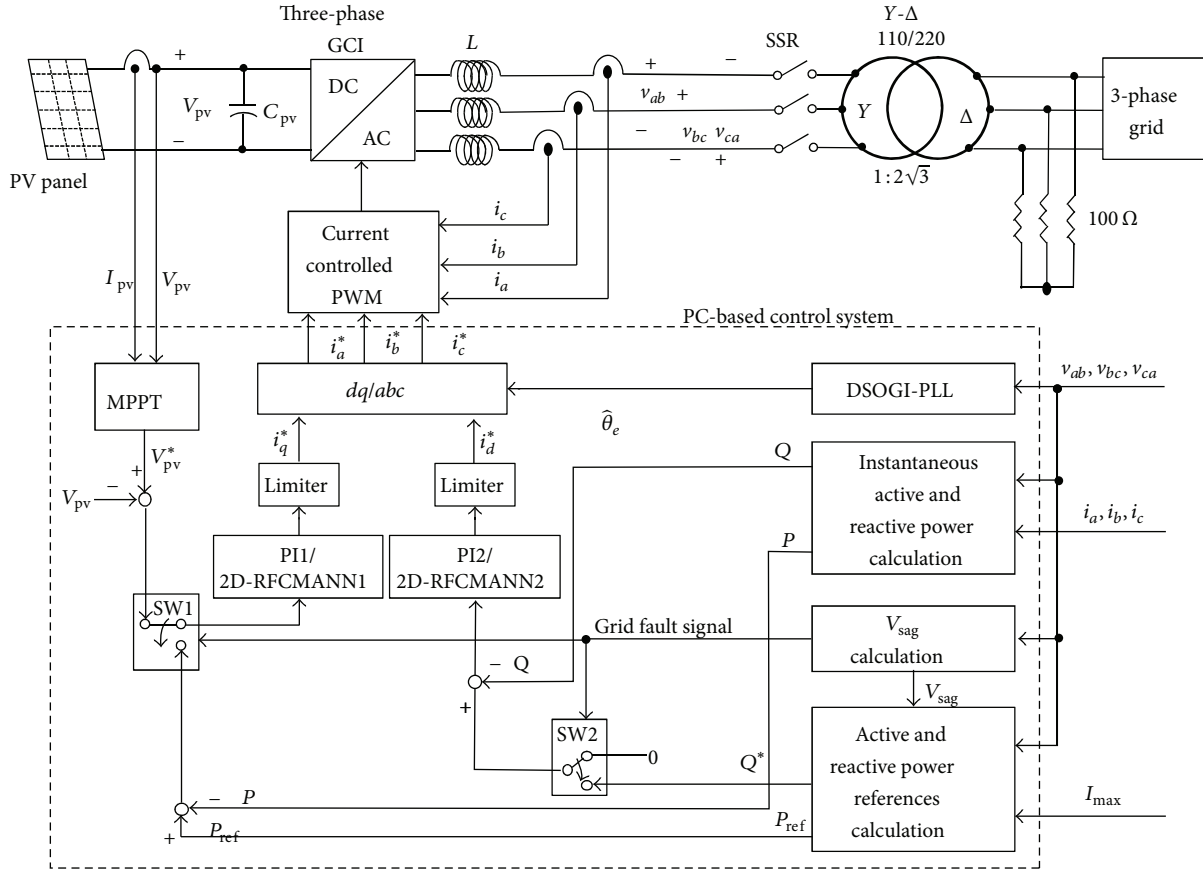


FIGURE 4: Schematic diagram of PC-based control system.

$$f_{pij_p}(N) = \exp\left(-\frac{(y_{pij_p}^2(N) - m_{pij_p})^2}{\sigma_{pij_p}^2}\right),$$

$$p = 1, 2, \quad i = 1, 2, \dots, n_i, \quad j_p = 1, 2, \dots, n_j, \quad (19)$$

$$y_{pij_p}^2(N) = x_p(N) + r_{pij_p} f_{pij_p}(N-1),$$

$$p = 1, 2, \quad i = 1, 2, \dots, n_i, \quad j_p = 1, 2, \dots, n_j,$$

where $f_{pij_p}(N)$ is the output of the j_p th block of the i th layer of the p th input variable; m_{pij_p} and σ_{pij_p} are the mean and standard deviation of the Gaussian function, respectively; r_{pij_p} represents the recurrent weight of the j_p th block of the i th layer for the p th input variable internal feedback unit; N denotes the time step; and $f_{pij_p}(N-1)$ represents the value of $f_{pij_p}(N)$ through time delay. Note that the memory term $f_{pij_p}(N-1)$ stores the past information of the 2D-RFCMANN network and performs the dynamic property. Considering the example shown in Figure 4(b), the 2D-RFCMANN has two input variables with three layers in the 2D-RFCMANN and four blocks in each layer.

Space 3 (receptive-field space). In this space, each block has three adjustable parameters, r_{pij_p} , m_{pij_p} , and σ_{pij_p} . The multidimensional receptive-field function is defined as

$$h_{ij_1j_2}(N) = f_{1ij_1}(N) f_{2ij_2}(N)$$

$$= \exp\left(-\frac{(y_{1ij_1}^2(N) - m_{1ij_1})^2}{\sigma_{1ij_1}^2}\right)$$

$$\times \exp\left(-\frac{(y_{2ij_2}^2(N) - m_{2ij_2})^2}{\sigma_{2ij_2}^2}\right) \quad (20)$$

$$i = 1, 2, \dots, n_i; \quad j_1, j_2 = 1, 2, \dots, n_j,$$

where $h_{ij_1j_2}(N)$ is associated with the i th layer and the j_1 th block for input x_1 and the j_2 th block for input x_2 according to the fuzzy rules in (12). The product is computed by using t -norm product in the antecedent part. An organization diagram of the 2D-RFCMANN is depicted in Figure 4(b). Areas formed by blocks, referred to as $f_{111}f_{211}$, $f_{112}f_{211}$, \dots and so forth, are called receptive fields (or hypercube).

Moreover, the number of receptive fields is equal to n_j^2 in each layer.

Space 4 (weight space). Each receptive-field area corresponds to a particular adjustable value in the weight space. The output of the weight memory can be described as

$$y_{ij_1j_2}^4(N) = w_{ij_1j_2}(N), \quad (21)$$

$$i = 1, 2, \dots, n_i; \quad j_1, j_2 = 1, 2, \dots, n_j,$$

where $y_{ij_1j_2}^4(N)$ is the output of the weight memory corresponding to $h_{ij_1j_2}(N)$ and $w_{ij_1j_2}(N)$ denotes the connecting weight value of the output associated with the j_1 th block of x_1 and the j_2 th block of x_1 in the i th layer.

Space 5 (output space). The output of the 2D-RFCMANN is the summation of the entire activated weighted field:

$$y_o^5(N) = \sum_{i=1}^{n_i} y_{ij_1j_2}^5(N), \quad (22)$$

$$y_{ij_1j_2}^5(N) = w_{ij_1j_2}(N) h_{ij_1j_2}(N),$$

where $y_{ij_1j_2}^5(N)$ is the product of the output of the weight memory and the output of receptive-field. Moreover, $y_o^5 = i_q^*$ for the active power control and $y_o^5 = i_d^*$ for the reactive power control in the GCI.

An example is demonstrated to show the relation between 2D-RFCMANN and its fuzzy inference system. As shown in Figure 3(b), if the inputs of 2D-RFCMANN fall within the state (3, 5), three reception fields are activated which are $H_1 = f_{111}f_{212}$, $H_2 = f_{122}f_{222}$, and $H_3 = f_{132}f_{233}$. Each hypercube of the reception-field space is subject to the respective weights w_{112} , w_{222} , and w_{323} in the weight space.

4.2. Online Learning Algorithm of 2D-RFCMANN. Since the online learning algorithms of the active and reactive power controls are the same, only the detailed derivation of the reactive power control is discussed in this study. To describe the online learning algorithm of the 2D-RFCMANN for the input command tracking using supervised gradient decent method, first the energy function E is defined as

$$E(N) = \frac{1}{2}(y^*(N) - y(N))^2 = \frac{1}{2}e^2(N), \quad (23)$$

where $e(N)$ represents the tracking error in the learning process of the 2D-RFCMANN for each discrete time N ; $y^*(N)$ and $y(N)$ represent the desired output and the current output of the system. Then the backpropagation learning algorithm is described as follows.

Space 5. The error term to be propagated is given by

$$\delta_o^5 = -\frac{\partial E}{\partial y_o^5(N)} = -\frac{\partial E(N)}{\partial y} \frac{\partial y}{\partial y_o^5(N)} = e(N) \frac{\partial y}{\partial y_o^5(N)}. \quad (24)$$

The weights are updated by the amount:

$$\Delta w_{ij_1j_2}(N) = -\eta_1 \frac{\partial E}{\partial w_{ij_1j_2}(N)}$$

$$= -\eta_1 \frac{\partial E}{\partial y_o^5(N)} \frac{\partial y_o^5(N)}{\partial w_{ij_1j_2}(N)} = \eta_1 \delta_o^5 h_{ij_1j_2}(N), \quad (25)$$

where the factor η_1 is the learning rate of memory weights. $w_{ij_1j_2}$ is updated according to the following equation:

$$w_{ij_1j_2}(N+1) = w_{ij_1j_2}(N) + \Delta w_{ij_1j_2}(N). \quad (26)$$

Space 2. Applying the chain rule, the update laws for m_{pij_p} , σ_{pij_p} , and r_{pij_p} are

$$\Delta m_{pij_p}(N) = -\eta_2 \frac{\partial E}{\partial m_{pij_p}} = -\eta_2 \frac{\partial E}{\partial y_o^5(N)} \frac{\partial y_o^5(N)}{\partial m_{pij_p}}$$

$$= \eta_2 \delta_o^5 y_{ij_1j_2}^5(N) \frac{2(y_{pij_p}^2(N) - m_{pij_p})}{\sigma_{pij_p}^2},$$

$$\Delta \sigma_{pij_p}(N) = -\eta_3 \frac{\partial E}{\partial \sigma_{pij_p}} = -\eta_3 \frac{\partial E}{\partial y_o^5(N)} \frac{\partial y_o^5(N)}{\partial \sigma_{pij_p}}$$

$$= \eta_3 \delta_o^5 y_{ij_1j_2}^5(N) \frac{2(y_{pij_p}^2(N) - m_{pij_p})^2}{\sigma_{pij_p}^3}, \quad (27)$$

$$\Delta r_{pij_p}(N) = -\eta_4 \frac{\partial E}{\partial r_{pij_p}} = -\eta_4 \frac{\partial E}{\partial y_o^5(N)} \frac{\partial y_o^5(N)}{\partial r_{pij_p}}$$

$$= \eta_4 \delta_o^5 y_{ij_1j_2}^5(N) \frac{2(y_{pij_p}^2(N) - m_{pij_p})}{\sigma_{pij_p}^2}$$

$$\times f_{1ij_p}(N-1),$$

where the factors η_2 , η_3 , and η_4 are the learning rates. m_{pij_p} , σ_{pij_p} , and r_{pij_p} are updated according to the following equation:

$$m_{pij_p}(N+1) = m_{pij_p}(N) + \Delta m_{pij_p}(N),$$

$$\sigma_{pij_p}(N+1) = \sigma_{pij_p}(N) + \Delta \sigma_{pij_p}(N), \quad (28)$$

$$r_{pij_p}(N+1) = r_{pij_p}(N) + \Delta r_{pij_p}(N).$$

Moreover, the exact calculation of the Jacobian of the system, $\partial y / \partial y_o^5(N)$, is difficult to be determined due to the unknown dynamics of the single-stage three-phase grid-connected PV system. To overcome this problem, a delta adaptation law is adopted as follows [18]:

$$\delta_o^5 \cong (y^* - y) + (\dot{y}^* - \dot{y}) = e + \dot{e}, \quad (29)$$

where \dot{y}^* and \dot{y} represent the first derivatives of y^* and y , respectively. Furthermore, the selection of the values of the

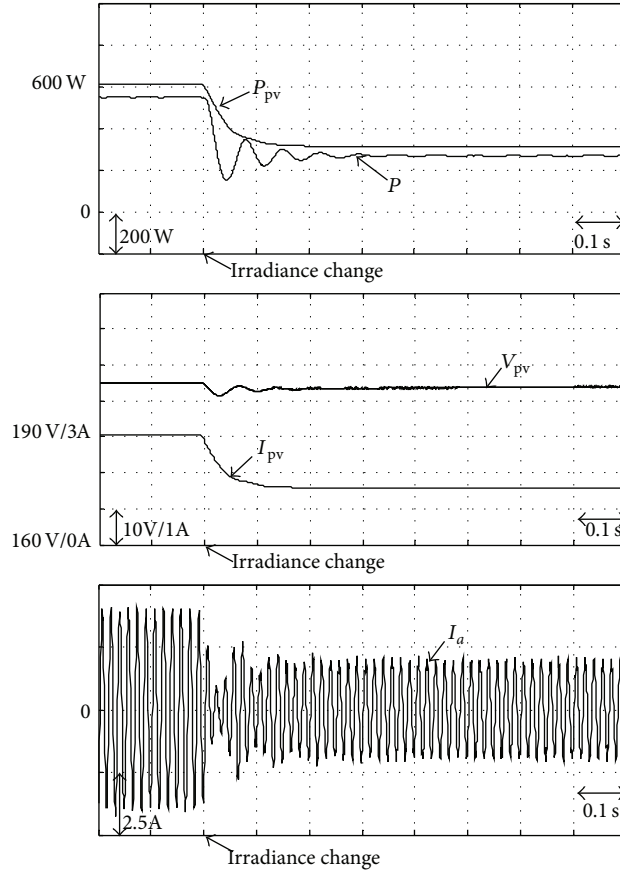


FIGURE 5: Experimental results of irradiance abrupt change using 2D-RFCMANN controller.

learning rate parameters of the 2D-RFCMANN has a significant effect on the network performance. Therefore, in order to train the 2D-RFCMANN effectively, the varied learning rates, which guarantee the convergence of the tracking errors based on the analysis of a discrete-type Lyapunov function, are derived as follows:

$$\begin{aligned} \eta_1 &= \frac{E(N)}{4 \left[\sum_{i=1}^{n_i} \left((\partial E / \partial y_o^5(N)) (\partial y_o^5(N) / \partial w_{ij_1 j_2}) \right)^2 + \varepsilon \right]}, \\ \eta_2 &= \frac{E(N)}{4 \left[\sum_{i=1}^{n_i} \left((\partial E / \partial y_o^5(N)) (\partial y_o^5(N) / \partial m_{pij_p}) \right)^2 + \varepsilon \right]}, \\ \eta_3 &= \frac{E(N)}{4 \left[\sum_{i=1}^{n_i} \left((\partial E / \partial y_o^5(N)) (\partial y_o^5(N) / \partial \sigma_{pij_p}) \right)^2 + \varepsilon \right]}, \\ \eta_4 &= \frac{E(N)}{4 \left[\sum_{i=1}^{n_i} \left((\partial E / \partial y_o^5(N)) (\partial y_o^5(N) / \partial r_{pij_p}) \right)^2 + \varepsilon \right]}, \end{aligned} \quad (30)$$

where ε is a positive constant. The derivation is similar to the one in [18] and is omitted in this study.

5. Experimental Results

The schematic diagram of the PC-based control system is depicted in Figure 4. The $\hat{\theta}_e$ is obtained by DSOGI-PLL block. The P and Q are obtained by the instantaneous active and reactive power calculation block shown in (4) and (5). The V_{sag} calculation block determines the value of V_{sag} and the grid fault signal is activated, while V_{sag} is greater than 0.1. The P_{ref} and Q^* are obtained by the active and reactive power references calculation block. The first PI controller (PI1) or the first 2D-RFCMANN (2D-RFCMANN1) is adopted for the control loop of V_{pv} or P to regulate the control output i_q^* . The control loop of Q introduces the second PI controller (PI2) or the second 2D-RFCMANN controller (2D-RFCMANN2) to regulate the control output i_d^* . Moreover, since the single-stage three-phase grid-connected PV system is a nonlinear system with uncertainties, the plant model is difficult to obtain by mathematical analysis or experimentation. Therefore, the parameters of PI controllers are tuned by trial and error in this study to achieve the best control performance considering the stability requirement. The transfer functions of these PI controllers which are adopted in this paper can be generally expressed as $k_{pn} + k_{in}/s$, $n = 1, 2$, where k_{pn} is the proportional gain and k_{in} is the integral gain. The gains of these PI controllers k_{p1} , k_{i1} , k_{p2} , and k_{i2} are tuned to be 1.2, 1, 1, and 1.2. Furthermore, both PI and 2D-RFCMANN

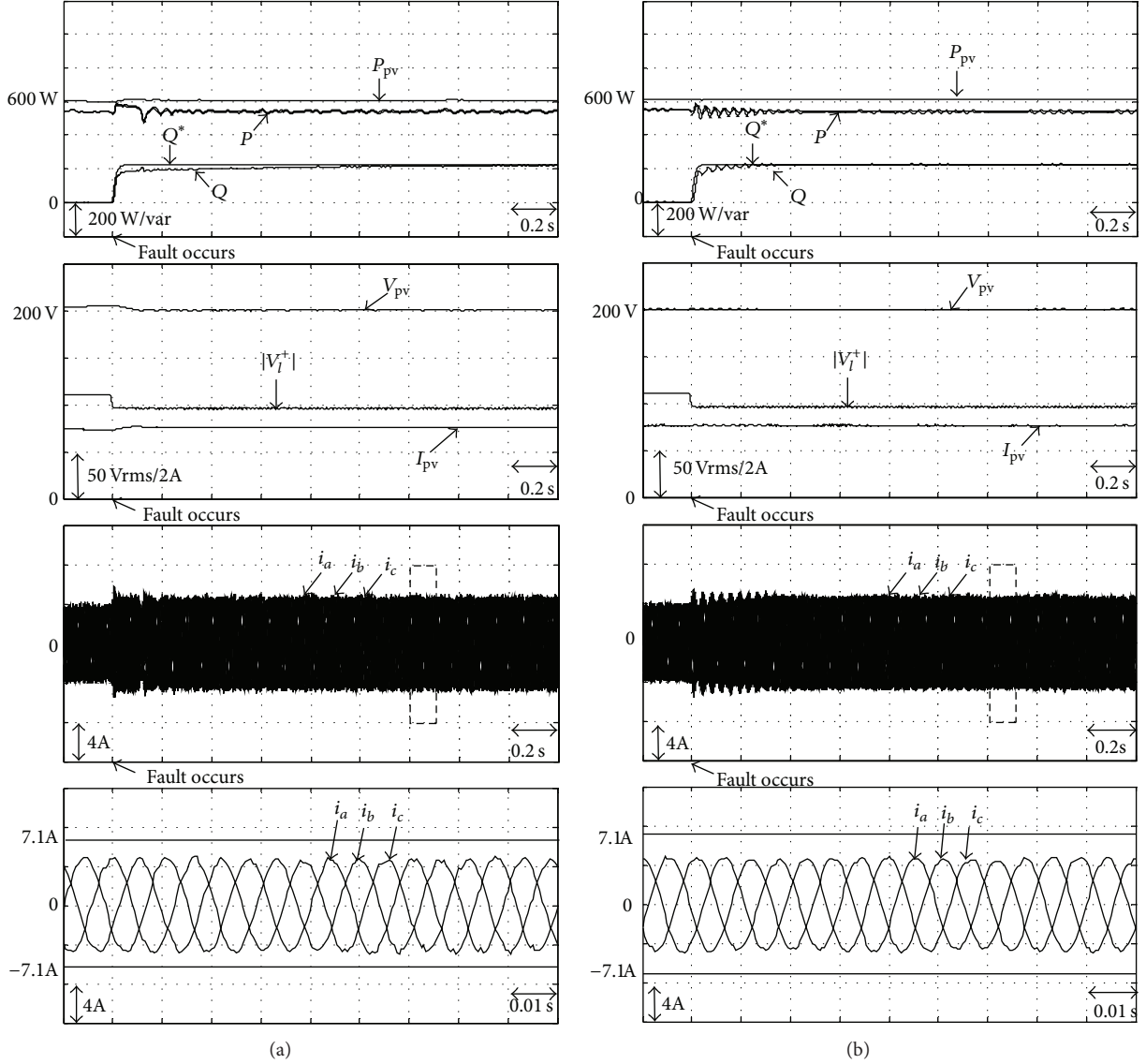


FIGURE 6: Experimental results of Case 1: (a) using PI controllers and (b) using 2D-RFCMANN controllers.

controllers are implemented in the experimentation for the comparison of the control performance. In order to measure the control performance of the mentioned controllers, the average tracking error T_{avg} , the maximum tracking error T_{MAX} , and the standard deviation of the tracking error T_{σ} for the reference tracking are defined as follows [18]:

$$T_d(N) = T^*(N) - T(N),$$

$$T_{\text{MAX}} = \max_N (|T_d(N)|), \quad T_{\text{avg}} = \frac{1}{m} \left(\sum_{N=1}^m T_d(N) \right),$$

$$T_{\sigma} = \sqrt{\frac{1}{m} \left(\sum_{N=1}^m (T_d(N) - T_{\text{avg}})^2 \right)},$$

(31)

where $T^*(N)$ is the N th value of the reference ($Q^*(N)$) and $T(N)$ is the N th value of the response ($Q(N)$). The comparison of the control performance can be demonstrated using the maximum tracking error and the average tracking error. The oscillation of the reference tracking can be measured by the standard deviation of the tracking error.

The emulated irradiance varying from 600 W/m^2 to 300 W/m^2 has been programmed in the PV panel simulator to evaluate the MPPT performance at normal state. The measured P , P_{pv} , V_{pv} , I_{pv} , and one of the line currents of GCI i_a are shown in Figure 5. In the beginning, P_{pv} , P , V_{pv} , and I_{pv} are 610 W , 546 W , 203.8 V , and 3.06 A , respectively, and the amplitude of i_a is 4.1 A . At $t = 0.2 \text{ s}$, the irradiance changes abruptly to 300 W/m^2 , and P_{pv} drops to 311 W . Then, P drops to 267 W ; V_{pv} drops to 201.6 V ; I_{pv} decreases to 1.6 A ; the amplitude of i_a reduces to 2.3 A . From the experimental results, when the 2D-RFCMANN1 controller is

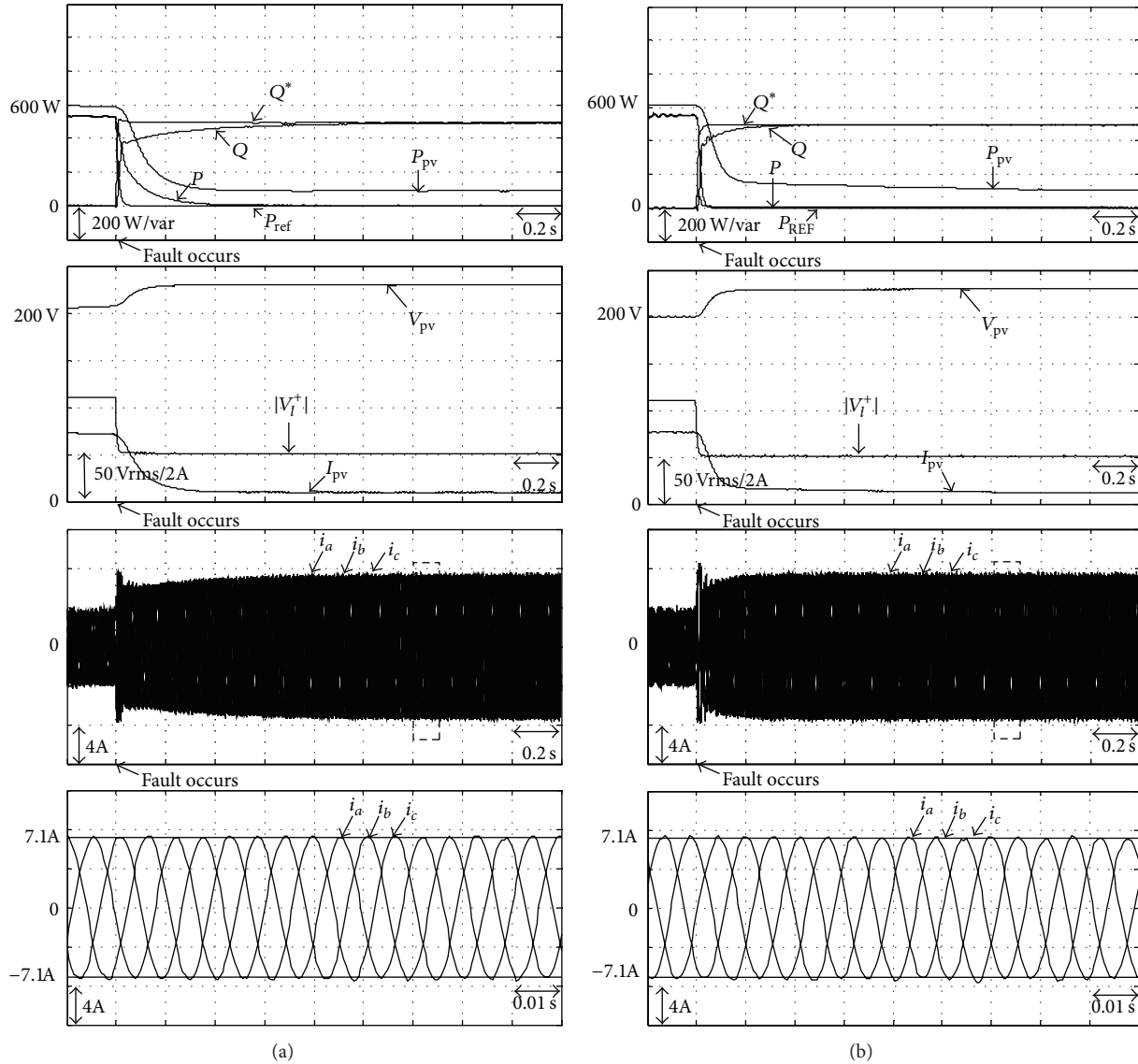


FIGURE 7: Experimental results of Case 2: (a) using PI controllers and (b) using 2D-RFCMANN controllers.

used, the settling time of P is about 0.3 s. Meanwhile, the total harmonic distortion (THD) of the current of the GSI is about 4.5%. The THD of the GCI is smaller than the THD regulation of IEEE 1547 standard. Therefore, the performances of the IC MPPT method satisfy the requirements of fast response and low THD for the proposed single-stage three-phase grid-connected PV system operating under normal condition.

Two cases of emulated grid faults with different voltage sags have been programmed in the ac power supplies to evaluate the behavior of the proposed PV system. The following grid faults at PCC are selected in this study: Case 1 two-phase ground fault with 0.2 pu voltage sag (sag type E) and Case 2 two-phase ground fault with 0.8 pu voltage sag (sag type E). In the experimentation, first, the grid line voltages are balanced and set at 1.0 pu. Then, at time $t = 0.2$ s, the sag happens and the reactive and active power controls are enabled.

Case 1. In this case, the measured P , Q , Q^* , V_{pv} , and I_{pv} and the measured three-phase currents are shown in Figure 6(a) for the PI controller and Figure 6(b) for the 2D-RFCMANN controller, respectively. In the beginning, P_{pv} is 608 W and P is 538 W due to the power losses in GCI. Moreover, the amplitude of the inverter output currents is 4 A. At $t = 0.2$ s, a two-phase ground fault occurs with 0.2 pu voltage sag on grid side and $|V_l^+|$ is 0.864 pu (95 Vrms) according to (13), where 1.0 pu is equal to 110 Vrms. V_{sag} and I_r^* are equal to 0.136 pu and 27.2% according to (15) and (14), respectively. By using (16) and (17), P^* and Q^* are determined to be 794 W and 224.6 var, respectively. Since P^* is greater than P , P_{ref} is set to P and eventually both P_{pv} and P are unchanged. Thus, Q rises to 224 var during the grid faults. Furthermore, the injection currents are approximately balanced and limited under 7.1 A peak value. From the experimental results, when the PI controllers are used, the settling time of Q is about 1.2 s.

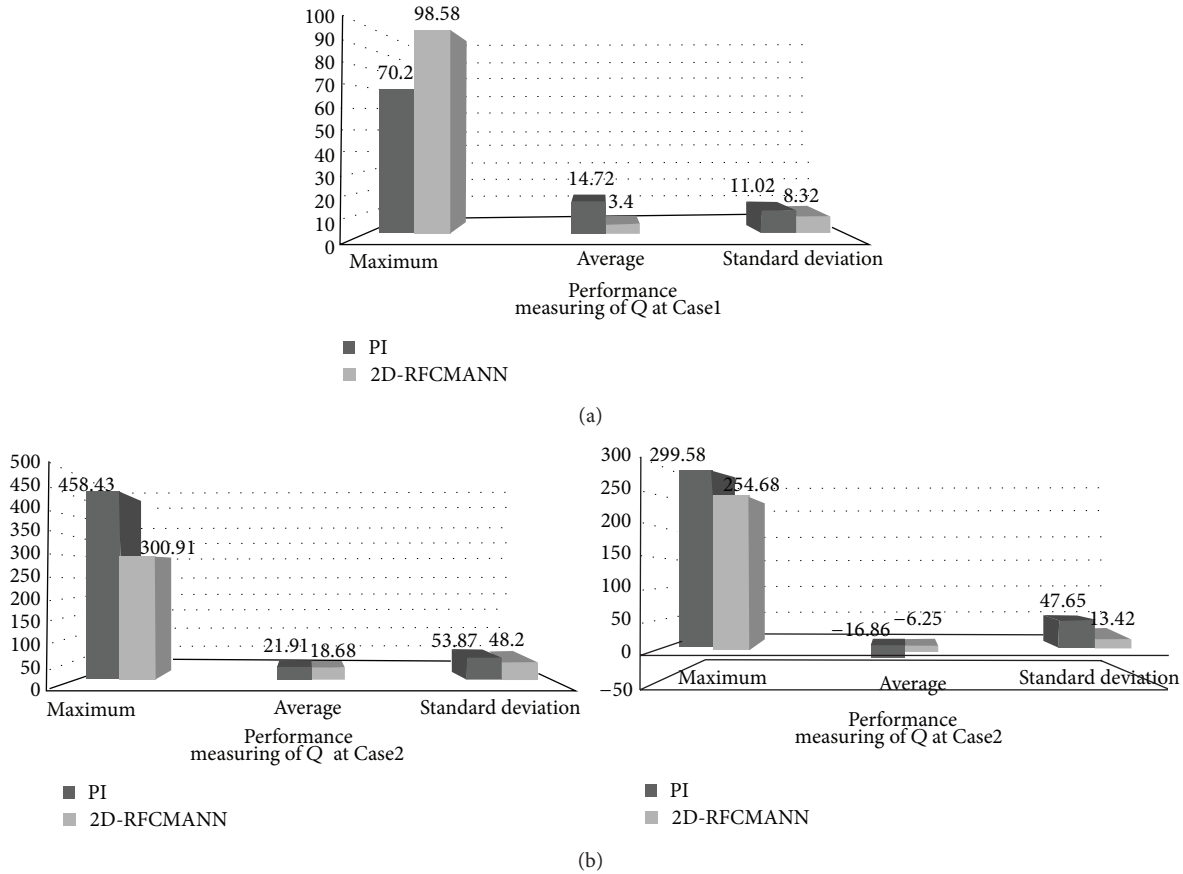


FIGURE 8: Performance measuring. (a) Performance measuring at Case 1. (b) Performance measuring at Case 2.

On the other hand, the settling time of Q is reduced to 0.3 s by using the 2D-RFCMANN controllers.

Case 2. In this case, the measured P , Q , P_{ref} , Q^* , V_{pv} , and I_{pv} and the measured three-phase currents are shown in Figure 7(a) for the PI controllers and Figure 7(b) for the 2D-RFCMANN controllers, respectively. At $t = 0.2$ s, two-phase ground fault occurs with 0.8 pu voltage sag on grid side. Thus, $|V_l^+|$ and I_r^* are equal to 0.462 pu and 100%, respectively, and P_{ref} is set to zero and the GCI gives up tracking the MPP. As a result, P_{pv} and P drop to 92 W and 2 W, respectively. Moreover, the GCI injects 493 var reactive power into the grid due to the 100% reactive current compensation. When either PI controller or 2D-RFCMANN controller is used, V_{pv} rises from 202 V to 230 V and I_{pv} drops from 3.1 A to 0.37 A due to the injected active power being set to zero. From the experimental results, when the PI controllers are used, the settling time of Q and P is about 1.0 s and 0.6 s, respectively. On the other hand, the settling time of Q and P is about 0.4s and 0.1s by using the 2D-RFCMANN controllers. Furthermore, the maximum injection currents are still limited within the maximum current limit.

From the experimental results of the previous two cases, it can be stated that the proposed single-stage three-phase grid-connected PV system has clearly demonstrated

its capabilities. These include the ability of dealing with voltage sags with satisfying the LVRT regulation and the ability of avoiding over current of the GCI. The performance measuring of the PI controller and 2D-RFCMANN controller for the command tracking is shown in Figure 8, using (31). From the resulted performance measuring of PI and 2D-RFCMANN controllers, the performances of 2D-RFCMANN controllers are superior to PI controllers.

6. Conclusions

This study has proposed an intelligent active and reactive power control scheme using 2D-RFCMANN for single-stage three-phase grid-connected PV system operating during grid faults. The mathematical analysis of the injected reactive power during the grid faults has been introduced. A new formula for evaluating the percentage of voltage sag has been proposed. The proposed formula, which is based on positive sequence voltage, is used to determine the ratio of the injected reactive current during grid faults for committing to the LVRT regulation. Moreover, the network structure, online learning algorithms, and learning rates of the proposed 2D-RFCMANN have been discussed in detail. The analyses of the experimental results indicate that the proposed scheme

is capable of providing reactive current support for a grid-connected PV system during grid faults. Furthermore, the control performance of the intelligent control scheme using 2D-RFCMANN is better than traditional control scheme using PI due to its online training of network parameters and the capability of parallel processing.

The contributions of this study are (1) the development of a single-stage three-phase grid-connected PV system with the compensation of reactive current during grid faults; (2) the design of the 2D-RFCMANN control scheme and its online learning algorithms with convergence analysis; and (3) the development of the 2D-RFCMANN controller in the reactive power and PV panel voltage control of a single-stage three-phase grid-connected PV system according to the LVRT regulation with the limitation of the maximum current output of GCI during grid faults.

Conflict of Interests

The authors declare that there is no conflict of interests regarding the publication of this paper.

Acknowledgment

The authors would like to acknowledge the financial support of the National Science Council of Taiwan, through Grant no. NSC 103-3113-P-008-001.

References

- [1] S.-Y. Wang, C.-L. Tseng, and S.-C. Chien, "Adaptive fuzzy cerebellar model articulation control for switched reluctance motor drive," *IET Electric Power Applications*, vol. 6, no. 3, pp. 190–202, 2012.
- [2] Y. N. Wang, T. Q. Ngo, T. L. Mai, and C. Z. Wu, "Adaptive recurrent wavelet fuzzy CMAC tracking control for de-icing robot manipulator," in *Proceedings of the World Congress on Engineering and Computer Science*, vol. 1, pp. 372–379, 2012.
- [3] C. Wen and M. Cheng, "Development of a recurrent fuzzy CMAC with adjustable input space quantization and self-tuning learning rate for control of a dual-axis piezoelectric actuated micromotion stage," *IEEE Transactions on Industrial Electronics*, vol. 60, no. 11, pp. 5105–5115, 2013.
- [4] C. T. Chiang and C. S. Lin, "Integration of CMAC and radial basis function techniques," in *Proceedings of the IEEE International Conference on Intelligent Systems for the 21st Century*, vol. 4, pp. 3263–3268, 1995.
- [5] C. Lin, H. Chen, and C. Lee, "A self-organizing recurrent fuzzy CMAC model for dynamic system identification," in *Proceeding of the IEEE International Conference on Fuzzy Systems*, vol. 2, pp. 697–702, July 2004.
- [6] M. H. J. Bollen, "Characterisation of voltage sags experienced by three-phase adjustable-speed drives," *IEEE Transactions on Power Delivery*, vol. 12, no. 4, pp. 1666–1671, 1997.
- [7] V. Ignatova, P. Granjon, and S. Bacha, "Space vector method for voltage dips and swells analysis," *IEEE Transactions on Power Delivery*, vol. 24, no. 4, pp. 2054–2061, 2009.
- [8] E.ON Netz GmbH, *Grid Code-High and Extra High Voltage*, E.ON Netz GmbH, Bayreuth, Germany, 2006.
- [9] M. Castilla, J. Miret, J. L. Sosa, J. Matas, and L. G. de Vicuña, "Grid-fault control scheme for three-phase photovoltaic inverters with adjustable power quality characteristics," *IEEE Transactions on Power Electronics*, vol. 25, no. 12, pp. 2930–2940, 2010.
- [10] P. Rodriguez, A. V. Timbus, R. Teodorescu, M. Liserre, and F. Blaabjerg, "Flexible active power control of distributed power generation systems during grid faults," *IEEE Transactions on Industrial Electronics*, vol. 54, no. 5, pp. 2583–2592, 2007.
- [11] J. Miret, M. Castilla, A. Camacho, L. G. De Vicuña, and J. Matas, "Control scheme for photovoltaic three-phase inverters to minimize peak currents during unbalanced grid-voltage sags," *IEEE Transactions on Power Electronics*, vol. 27, no. 10, pp. 4262–4271, 2012.
- [12] C. T. Lee, C. W. Hsu, and P. T. Cheng, "A low-voltage ride-through technique for grid-connected converters of distributed energy resources," *IEEE Transactions on Industry Applications*, vol. 47, no. 4, pp. 1821–1832, 2011.
- [13] A. Camacho, M. Castilla, J. Miret, J. C. Vasquez, and E. Alarcon-Gallo, "Flexible voltage support control for three-phase distributed generation inverters under grid fault," *IEEE Transactions on Industrial Electronics*, vol. 60, no. 4, pp. 1429–1441, 2013.
- [14] A. Nicastrì and A. Nagliero, "Comparison and evaluation of the PLL techniques for the design of the grid-connected inverter systems," in *Proceedings of the IEEE International Symposium on Industrial Electronics (ISIE '10)*, pp. 3865–3870, July 2010.
- [15] R. Teodorescu, M. Liserre, and P. Rodriguez, *Grid Converters for Photovoltaic and Wind Power Systems*, John Wiley & Sons, New York, NY, USA, 2011.
- [16] R. A. Mastromauro, M. Liserre, and A. Dell'Aquila, "Control issues in single-stage photovoltaic systems: MPPT, current and voltage control," *IEEE Transactions on Industrial Informatics*, vol. 8, no. 2, pp. 241–254, 2012.
- [17] F. Wang, J. L. Duarte, and M. A. M. Hendrix, "Pliant active and reactive power control for grid-interactive converters under unbalanced voltage dips," *IEEE Transactions on Power Electronics*, vol. 26, no. 5, pp. 1511–1521, 2011.
- [18] F. J. Lin, M. S. Huang, P. Y. Yeh, H. C. Tsai, and C. H. Kuan, "DSP-based probabilistic fuzzy neural network control for li-ion battery charger," *IEEE Transactions on Power Electronics*, vol. 27, no. 8, pp. 3782–3794, 2012.



Hindawi

Submit your manuscripts at
<http://www.hindawi.com>

